Chemical Science

ROYAL SOCIETY OF CHEMISTRY

EDGE ARTICLE

View Article Online
View Journal | View Issue

Check for updates

Cite this: *Chem. Sci.*, 2026, **17**, 6147

All publication charges for this article have been paid for by the Royal Society of Chemistry

Efficient pure-red multiple resonance emitter based on a donor planarization strategy

Linjie Li,[a] Yincai Xu, *[a] Dongyue Zhang,[b] Yupei Qu,[a] Yue Wang[a] and Chenglong Li *[a]

Received 28th November 2025
Accepted 26th January 2026

DOI: 10.1039/d5sc09303a

rsc.li/chemical-science

Efficient pure-red multiple resonance thermally activated delayed fluorescence (MR-TADF) emitters compatible with vacuum thermal evaporation remain scarce, which hampers the development of wide color gamuts for ultra-high-definition displays. The prevailing approach connecting one or more donors to the highest occupied molecular orbital positions of the MR core *via* single bonds suffers from inherent torsional flexibility, which results in the limited red shift, large molecular weight and broadened emission bandwidth. Herein, we present a donor planarization strategy in which the donor is intramolecularly fused with an MR core to generate a planar structural framework. This strategy not only enhances π-conjugation and the long-range charge transfer effect to enable a significant red shift in emission, but also improves molecular planarity to narrow the emission bandwidth. The proof-of-concept emitter, **RBN-ICz**, achieves a 96 nm red shift (from 519 to 615 nm) and a reduced emission bandwidth from 0.18 to 0.15 eV compared to parent molecule ***m*-Cz-BNCz**. Notably, **RBN-ICz** exhibits the lowest molecular weight among all reported red MR-TADF materials. The **RBN-ICz**-based organic light-emitting diode (OLED) achieves an external quantum efficiency (EQE) of 34.1% with Commission Internationale de l'Éclairage (CIE) coordinates of (0.67, 0.33), fully meeting the National Television System Committee (NTSC) red standard. This work offers an effective route for the development of high-efficiency, narrowband red MR-TADF emitters.

Introduction

Narrowband emitters can profoundly enhance the resolution and color saturation of displays, playing an indispensable role in the evolution of ultra-high-definition organic light-emitting diode (OLED) technology.[1] Recently, multiple resonance (MR) emitters based on 1,4-azaboryl BN-heteroarenes have demonstrated efficient narrowband thermally activated delayed fluorescence (TADF), and impressive progress has been made in the molecular synthesis and material applications within blue[2] and green[3] emission regions. However, the quest to construct high-performance MR-TADF emitters capable of accessing red emission (>600 nm) remains an enduring and formidable challenge.

A canonical paradigm for red-shifting the emission spectrum is to introduce a donor into the highest occupied molecular orbital (HOMO) position of the well-documented MR parent molecule BNCz through a single bond.[4] This strategy can modulate the HOMO energy level while keeping the lowest occupied molecular orbital (LUMO) relatively unchanged, thereby reducing the energy gap (E_{gap}) and causing bathochromic emission (Scheme 1a).[5] The corresponding molecular design typically focuses on increasing the number of donor units and varying donor identity (Scheme 1b).[6] For instance, Yasuda *et al.* incorporated two 3,6-di-*tert*-butyl-9*H*-carbazole (*t*Cz) units into the BNCz skeleton, achieving a 67 nm red shift, with yellow emission peaking at 549 nm and a full-width at half-maximum (FWHM) of 0.17 eV;[7] Yang *et al.* introduced a phenoselenazine donor, resulting in a 38 nm red shift, with pure-green emission peaking at 519 nm and a FWHM of 0.23 eV.[8] Although this method can achieve red shift, the introduction of strong intramolecular charge transfer will destroy the resonance structure to a certain extent and widen the FWHM, so it is still very challenging to achieve narrowband red emission. This limitation primarily stems from the intrinsic torsional flexibility of donors attached to the MR core *via* a rotatable single bond, which typically leads to a large donor–core dihedral angle. This geometric constraint has two direct photophysical consequences on emission. First, reduced donor–core orbital overlap suppresses long-range charge-transfer (LRCT) characteristic and restricts π-conjugation, thereby restricting the attainable red shift.[9] Second, torsional flexibility increases the ground state (S_0)–the lowest singlet excited (S_1) reorganization energy and strengthens vibronic coupling, resulting in broadened bandwidth.[10] Adding multiple donors could facilitate further

---

[a] State Key Laboratory of Supramolecular Structure and Materials, College of Chemistry, Jilin University, Changchun 130012, P. R. China. E-mail: chenglongli@jlu.edu.cn; ycxu17@mails.jlu.edu.cn

[b] School of Chemistry and Pharmaceutical Engineering, Jilin Institute of Chemical Technology, Jilin 132022, P. R. China

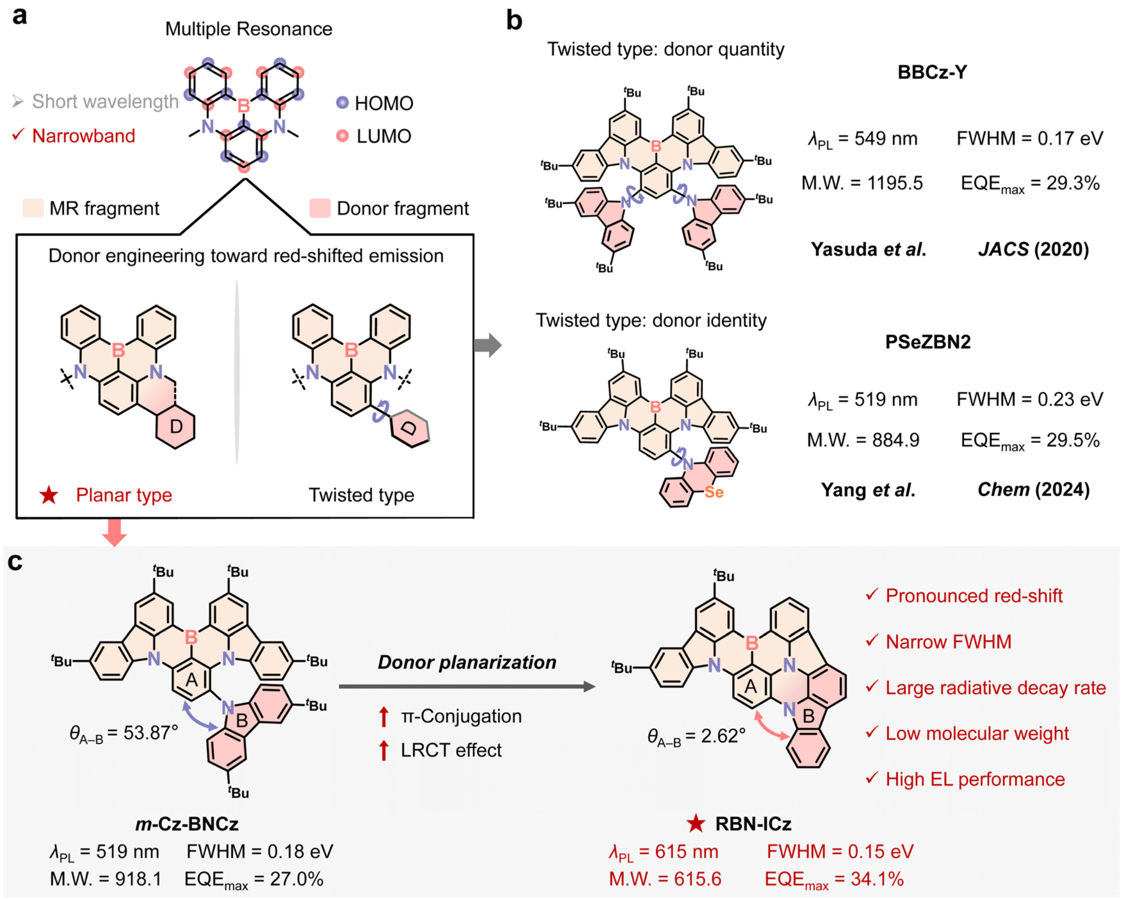

Scheme 1 (a) Donor engineering toward red-shifted emission based on the MR framework. (b) Representative examples of single-bonded donor substitution with twisted donors. (c) Molecular design strategy based on the incorporation of a planarized donor into the MR framework.

red shift, but the concomitant increase in molecular weight often compromises compatibility with vacuum thermal evaporation processes for OLEDs.[11] Despite numerous efforts to engineer donor substitution, most research prioritizes donor quantity and identity, while conformational control, particularly the planarity of the donor–core junction, has gained insufficient attention. This often-overlooked structural factor plays a crucial role in excited-state modulation.[12] Without explicit conformational control, donor-substitution strategies typically yield only moderate bathochromic shifts, struggling to achieve significant shifts into the pure-red region.

To address these challenges in developing narrowband red emitters, we focus on conformational manipulation of the donor–core junction and implement a donor planarization strategy, enabling a significant bathochromic shift to the pure-red region. Unlike conventional donor-substitution approaches, which connect donors to the MR core *via* a rotatable single bond, our strategy integrates the donor intramolecularly into the BNCz core to form an aromatic amine backbone composed of planar building blocks 11,12-dihydroindolo[2,3-*a*]carbazole (ICz) and *t*Cz, coordinated with a boron atom, resulting in a rigid, near-coplanar emitter, **RBN-ICz** (Scheme 1c). Compared to the donor–core dihedral angle of 53.87° in ***m*-Cz-BNCz** with a single-bonded donor, the donor–core dihedral angle in **RBN-ICz** is compressed to 2.62°, leading to a markedly improved near-coplanar geometry. The increased planarity extends the π-conjugation and enhances the LRCT effect, significantly enabling a substantial red-shift into the pure-red region. The emission wavelength shifts from 519 nm (pure-green emission for ***m*-Cz-BNCz**) to 615 nm (pure-red emission for **RBN-ICz**), resulting in a 96 nm red shift and narrowing of the FWHM from 0.18 eV to 0.15 eV. The corresponding OLED exhibits a maximum external quantum efficiency (EQE) of 34.1% with Commission Internationale de l'Éclairage (CIE) coordinates of (0.67, 0.33), fully meeting the National Television System Committee (NTSC) red emission standard (0.67, 0.33) and approaching the BT.2020 red primary at (0.708, 0.292). This planarization strategy significantly reduces the complexity of red light-emitting molecular design, rendering **RBN-ICz** one of the smallest molecular weight red B,N-containing MR materials reported to be suitable for vacuum thermal evaporation. This provides a new approach for the development of high-efficiency, structurally simple, and narrowband red-emitting materials.

Results and discussion

The tandem one-pot lithiation–borylation–annulation sequence using halogenated aromatic amine precursors is a classic synthetic methodology for constructing B,N-containing MR frameworks. Depending on the relative position of the halogen

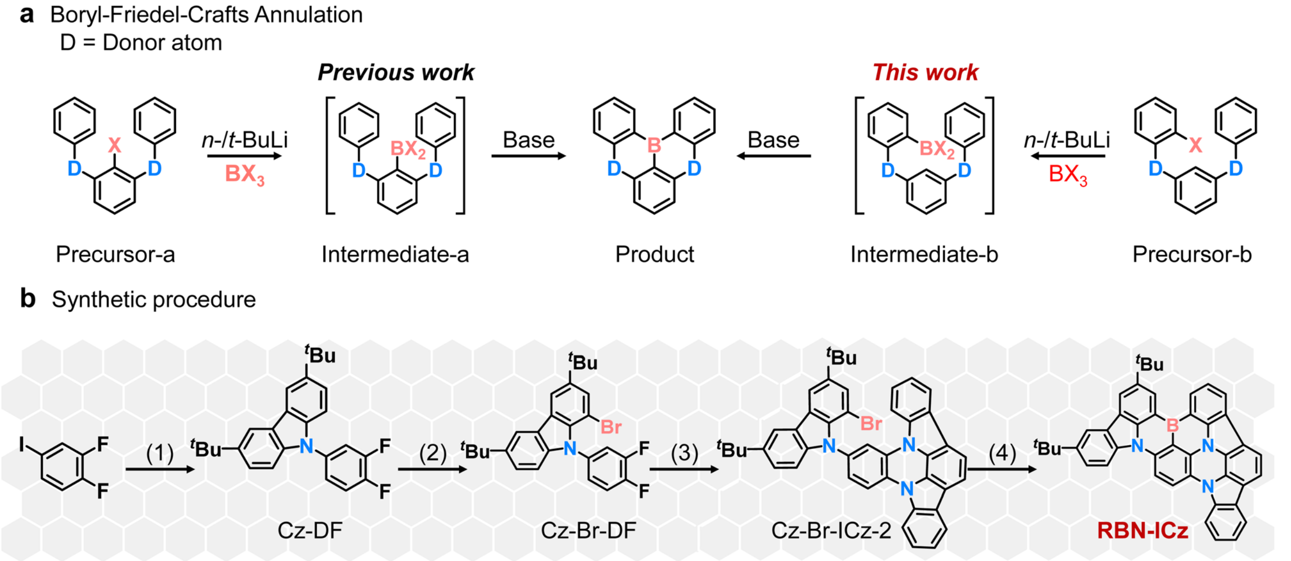

Fig. 1 (a) Boryl–Friedel–Crafts annulation: comparison of reaction design in previous work and this work. (b) Synthetic procedure of **RBN-ICz**: (1) Cu, K_2CO_3, 18-Crown-6, *o*-DCB; (2) NBS, DMF; (3) Cs_2CO_3, DMF; (4) (1) *n*-BuLi, *t*-BuPh, (2) BBr_3, and (3) DIPEA.

with respect to the donor sites, the precursor design can generally be categorized into two connectivity patterns, namely donor–halogen–donor (D–X–D) and donor–donor–halogen (D–D–X) (X = Cl, Br, I) (Fig. 1a).[13] In both cases, lithium–halogen exchange followed by borylation affords the corresponding borylated intermediate (intermediate-a or intermediate-b), which subsequently undergoes base-promoted intramolecular annulation to deliver the boron-embedded polycyclic product. Guided by this framework, and after systematic optimization of the precursor construction, we selected the intermediate-b pathway for the synthesis of **RBN-ICz** (Fig. 1b). As shown in Fig. 1b, the synthesis proceeds in four steps. First, 1,2-difluoro-4-iodobenzene and *t*Cz were coupled under copper-catalyzed Ullmann conditions to afford Cz-DF. Second, bromination of Cz-DF with *N*-bromosuccinimide (NBS) furnished the key intermediate Cz-Br-DF. Third, nucleophilic aromatic substitution between Cz-Br-DF and ICz provided Cz-Br-ICz-2. Finally, Cz-Br-ICz-2 was converted into **RBN-ICz** *via* the one-pot lithiation–borylation–annulation. The structures of all intermediates and target compounds were fully characterized by NMR and mass spectrometry (Fig. S1–S11). Based on cyclic voltammetry (CV) measurement, the LUMO energy level was estimated to be −2.83 eV for **RBN-ICz** (Fig. S12). Based on the LUMO energy level and optical bandgap (E_{gap}) calculated from the onset of the UV-vis absorption spectrum of **RBN-ICz**, the HOMO energy level was estimated to be −4.83 eV. Thermogravimetric analysis (TGA) of **RBN-ICz** reveals a decomposition temperature (T_d, corresponding to 5% weight loss) of 499 °C, which makes it suitable for OLED manufacturing by the vacuum thermal deposition process (Fig. S13).

To comprehensively elucidate the differences in geometry and the electronic structure between ***m*-Cz-BNCz** and **RBN-ICz**, theoretical investigations were performed by employing density functional theory (DFT) and time-dependent density functional theory (TD-DFT) calculations (Fig. 2). The optimized geometric structures reveal substantial conformational differences between their respective donor units (Fig. S14). Specifically, the *t*Cz donor unit in ***m*-Cz-BNCz** exhibits a pronounced twist relative to the BNCz core.[14] In contrast, the ICz donor unit in **RBN-ICz** is highly planar, enhancing overall molecular planarity. These structural differences directly impact the spatial distribution of frontier molecular orbitals (FMOs). The HOMO of ***m*-Cz-BNCz** is distributed across the distorted *t*Cz donor and the BNCz fragment, while the LUMO is almost completely localized on the BNCz core. The planar configuration of **RBN-ICz** promotes extensive orbital delocalization, resulting in a wider distribution of the HOMO across the donor ICz and the BNCz core.[15] Furthermore, the LUMO remains primarily localized on the BNCz core, but some electron density also appears on ICz. These differences in orbital distribution are reflected in their respective FMO energy levels. The HOMO and LUMO energy levels of ***m*-Cz-BNCz** were calculated to be −4.90 and −1.82 eV, respectively, while those of **RBN-ICz** were −4.65 and −1.92 eV. The larger difference in HOMO energy levels can be explained by molecular orbital theory, which emphasizes that greater orbital overlap indicates stronger conjugation. Therefore, when the molecular planarity is optimized, the p-orbital of the sp^2-hybridized nitrogen atom can be well aligned with the p-orbital involved in the adjacent π-bond, thereby maximizing lateral orbital overlap (Fig. S15).[16] This enhances electron delocalization through enhanced p–π conjugation, stabilizes the conjugated system, and lowers the overall energy of the molecular system. This occurs because electrons flow within the delocalized large π-bond, resulting in lower energy compared to isolated p-/π-orbitals. As a result, the HOMO–LUMO energy gap is narrowed from 3.08 eV in ***m*-Cz-BNCz** to 2.73 eV in **RBN-ICz**, which is expected to lower the E_{gap} and drive a significant bathochromic shift into the red region.

To quantitatively evaluate the impact of donor planarization on molecular orbital composition, charge decomposition

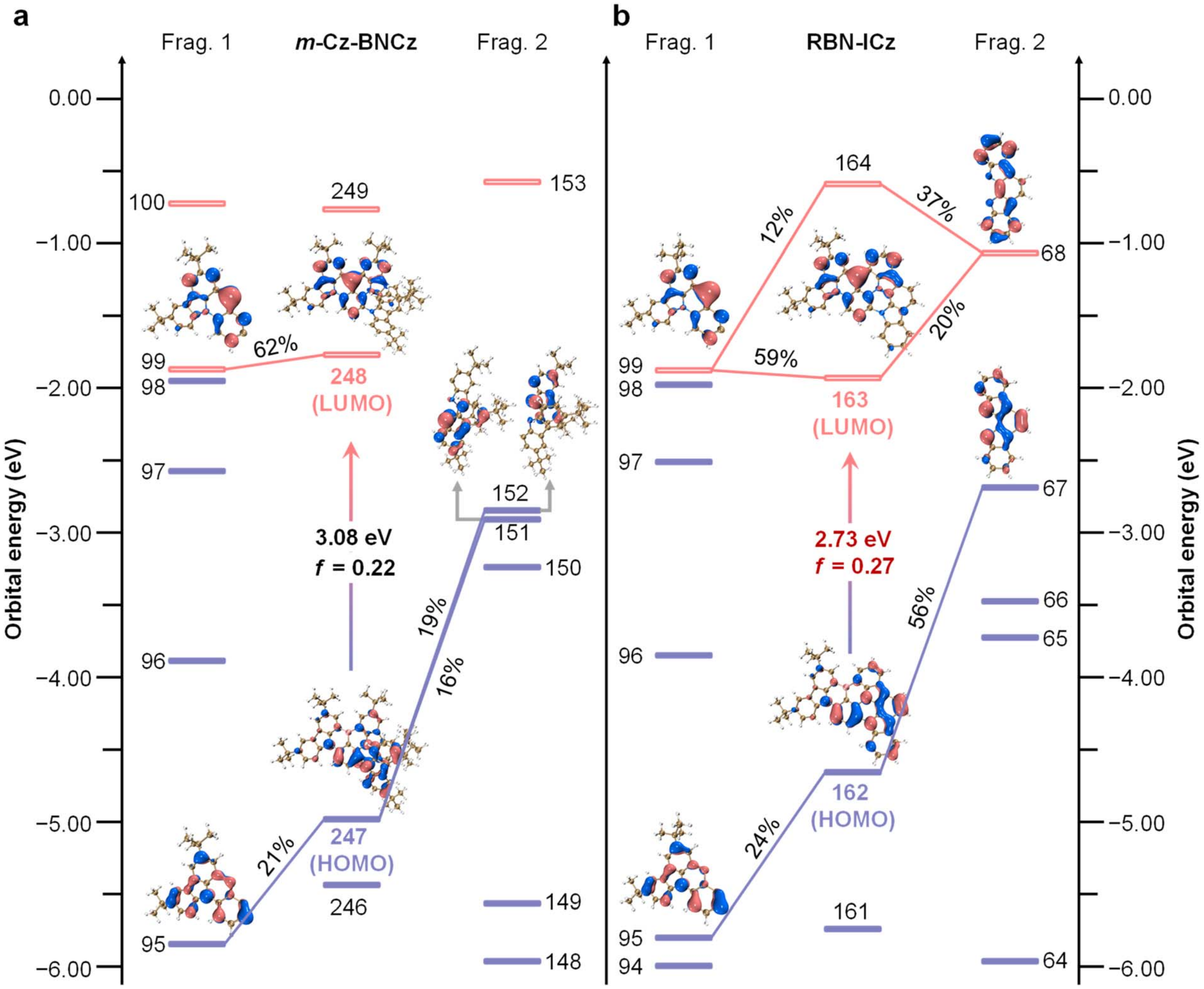

Fig. 2 Fragment molecular orbital analysis illustrating the effect of donor planarization on LRCT characteristics and orbital distributions. (a) *m*-Cz-BNCz with a twisted donor. (b) RBN-ICz with a planarized donor.

analysis (CDA) was performed by partitioning each molecule into two fragments: fragment 1 and fragment 2 (Fig. S16).[17] CDA reveals that fragment 2 contributes only 35% to the HOMO of ***m*-Cz-BNCz**, owing to the significant torsional decoupling between fragments 1 and 2. Due to the substantial dihedral angle between fragments 1 and 2, π-orbital overlap is restricted, partially impeding electron delocalization toward fragment 1 and consequently stabilizing the HOMO at a relatively deep energy level (Fig. 2a). In contrast, the planarized ICz donor in **RBN-ICz** forms an effectively continuous conjugated pathway with fragment 1, resulting in improved electron-donating capacity. This is evidenced by the approximately 56% HOMO composition on fragment 2 and 24% on fragment 1, collectively elevating the HOMO energy level (Fig. 2b). Regarding the LUMO distribution, ***m*-Cz-BNCz** predominantly features MR-centered antibonding orbitals (approximately 62% on fragment 1), wherein the constrained π-conjugation limited π* orbital delocalization, yielding a relatively high LUMO energy.[18] Conversely, the LUMO of **RBN-ICz** was jointly composed of contributions from fragment 1 (59%) and ICz's antibonding orbitals (20%). The planar configuration of ICz effectively expanded the electron delocalization pathway, more evenly dispersing electron density across the enlarged π-conjugated network and lowering the LUMO energy. In summary, donor planarization substantially enhanced the intramolecular π-conjugation and LRCT effect. By synergistically increasing the HOMO energy level and decreasing the LUMO energy level, the molecular energy gap is markedly reduced. These results support donor planarization as a pivotal design approach for longer-wavelength emitters without compromising their intrinsic MR characteristics.

To elucidate the fundamental structural differences prior to assessing the impact of donor planarization on the photophysical properties, we first conducted a quantitative analysis of molecular planarity using the molecular planarity parameter (MPP).[19] Compared to ***m*-Cz-BNCz**, which exhibits an MPP value of 1.34 Å, the MPP of **RBN-ICz** is significantly reduced to 0.42 Å—one of the lowest reported values among B,N-containing MR systems—indicating that **RBN-ICz** possesses a nearly perfectly planar molecular backbone (Fig. 3a). In addition, the electrostatic potential (ESP) was evaluated to probe the spatial distribution of surface potential (Fig. 3b).[20] While ***m*-Cz-BNCz** shows

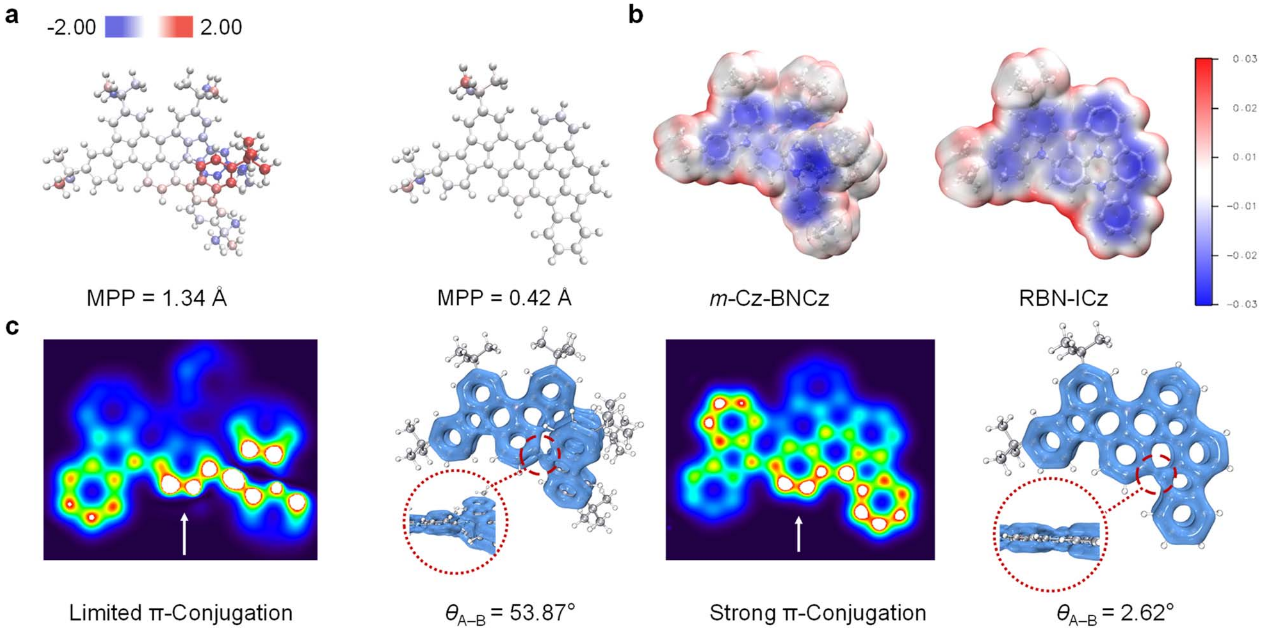

Fig. 3 Structural analysis revealing the impact of donor planarization on molecular conformation and π-conjugation. (a) Molecular planarity parameter (MPP). (b) Electrostatic potential (ESP) distributions. (c) π-Electron delocalization and dihedral angle (θ_{A-B}) comparison between ***m*-Cz-BNCz** and **RBN-ICz**.

a localized ESP pattern concentrated around the donor moiety, **RBN-ICz** exhibits a more homogeneous ESP distribution across the entire molecule, further indicating enhanced electronic delocalization enabled by planarization. To further investigate the influence of planarization on π-electron delocalization, we calculated the Localized Orbital Locator for π-electrons (LOL-π) distributions for both compounds (Fig. 3c).[21] In ***m*-Cz-BNCz**, the π-electron density between the *t*Cz donor and the BNCz core is significantly disrupted due to a torsional angle of 53.87°, resulting in a distinct discontinuity on the LOL-π isosurface. In contrast, **RBN-ICz**, with a torsional angle of only 2.62° between the ICz donor and the MR core, displays a continuous π-electron distribution across the entire donor–acceptor interface, reflecting a pronounced enhancement in π-conjugation. This distinction is further corroborated by *xy*-plane heatmap projection of the LOL-π distribution, which reveals a broader and more delocalized conjugated network in **RBN-ICz** compared to ***m*-Cz-BNCz**. The electronic consequences of donor planarization are further evidenced by the difference density plots between S_0 and S_1 states (Fig. S17). In **RBN-ICz**, the electron density depletion (green) and increment (blue) regions span the MR core, in stark contrast to ***m*-Cz-BNCz**, where excitation-induced electron redistribution is more localized. This suggests that **RBN-ICz** exhibits more efficient intramolecular charge transfer in the excited state.[22] The hole–electron analysis indicates that both compounds retain the characteristic MR-type excited-state features with substantial hole–electron overlap. Compared with ***m*-Cz-BNCz**, **RBN-ICz** exhibits a more spatially extended hole–electron distribution and a broader overlap region, consistent with an increased π-conjugation participation enabled by donor planarization (Fig. S18). Moreover, the calculated S_1 energy of **RBN-ICz** is significantly reduced (2.28 eV) compared to that of ***m*-Cz-BNCz** (2.59 eV), further supporting the pronounced red-shift in its emission spectrum. Collectively, these results demonstrate that donor planarization not only improves molecular coplanarity and π-conjugation, but also enhances orbital overlap and excited-state delocalization.

The fundamental photophysical properties of compounds ***m*-Cz-BNCz** and **RBN-ICz** were systematically investigated in toluene solution (Fig. 4a and d). Compared to the absorption maximum of ***m*-Cz-BNCz** at 484 nm, **RBN-ICz** exhibits a markedly red-shifted absorption peak at 582 nm, which can be attributed to its enhanced LRCT effect. Correspondingly, the E_g is significantly reduced from 2.42 eV for ***m*-Cz-BNCz** to 2.00 eV for **RBN-ICz**. Upon photoexcitation at 365 nm, **RBN-ICz** displays a pure-red emission at 615 nm, with a FWHM of 44 nm (0.15 eV) (Table 1). This represents a substantial red-shift of 96 nm relative to ***m*-Cz-BNCz**, which emits at a shorter wavelength (519 nm) and exhibits a broader FWHM (38 nm/0.18 eV). This spectral red-shift and FWHM narrowing are achieved solely through donor planarization, without the introduction of additional donor units. The Stokes shifts of the two compounds ***m*-Cz-BNCz** and **RBN-ICz** are 35 nm and 33 nm, respectively, indicating similar excited-state relaxation behavior. Root-mean-square deviation (RMSD) analysis between S_0 and S_1 geometries reveals a substantially smaller structural distortion for **RBN-ICz** (0.043 Å) compared to ***m*-Cz-BNCz** (0.152 Å) (Fig. S19), further confirming the rigidity imparted by the planarized donor framework, which underpins its narrowband emission properties.[23] Solvatochromic studies in solvents ranging from *n*-hexane to tetrahydrofuran show progressive emission red-shifts ($\Delta\lambda_{max} = 13$ and 31 nm) and spectral broadening (ΔFWHM = 12 and 34 nm) for ***m*-Cz-BNCz** and **RBN-ICz**, respectively (Table S1

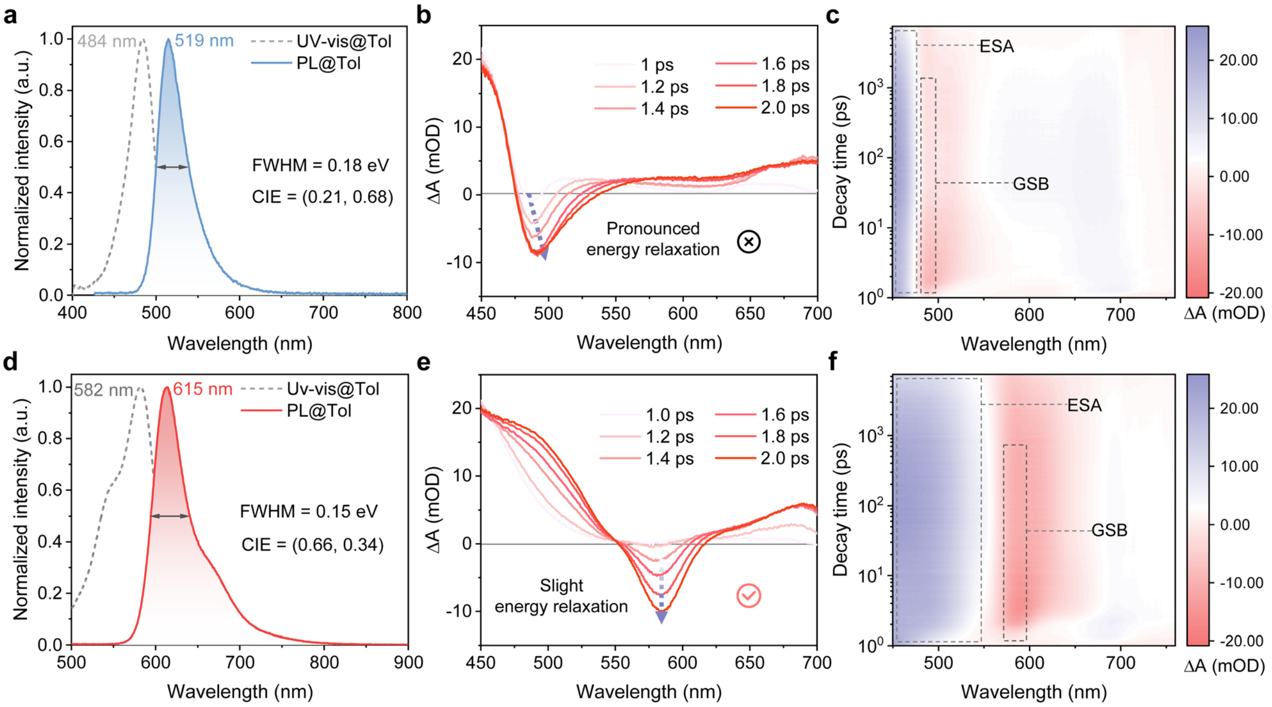

Fig. 4 (a and d) Absorption and fluorescence spectra; (b and e) species-associated spectra from global analysis of fs-transient absorption; (c and f) time–wavelength Δ*A* maps highlighting GSB and ESA; (a–c) ***m*-Cz-BNCz** and (d–f) **RBN-ICz**.

and Fig. S20). These trends reflect the consistently stronger LRCT properties exhibited by **RBN-ICz**, which is in good agreement with theoretical predictions. Overall, these results demonstrate that donor planarization serves as an effective molecular strategy for modulating π-conjugation and controlling the nature of charge-transfer excited states. Moreover, low-temperature photoluminescence spectroscopy of **RBN-ICz** in toluene reveals a small singlet–triplet energy gap ($\Delta E_{ST} = 0.16$ eV) (Fig. S21), suggesting the prospect of efficient reverse intersystem crossing (RISC) and TADF behavior.

Subsequently, femtosecond-transient absorption (fs-TA) was used to investigate the singlet-excited-state dynamics (Fig. 4 and S22). As shown in Fig. 4, both compounds display similar fs-TA fingerprints: a ground-state bleach (GSB) near the steady-state absorption and excited-state absorption (ESA) assignable to $S_1 \rightarrow S_n$. For ***m*-Cz-BNCz**, the GSB minimum undergoes a dynamic red shift of ~10 nm within 1–2 ps with a rapid decay of the S_1' ESA (Fig. 4b and c), indicating more pronounced energy/structural relaxation on the S_1 surface. By contrast, **RBN-ICz** shows only slight or negligible peak displacement over the same window (Fig. 4e and f), consistent with a more constrained excited-state geometry and smaller relaxation. These observations rationalize the maintenance of narrowband emission despite the large red shift. These results substantiate that donor planarization suppresses torsional flexibility, enabling a large bathochromic shift with minimal excited-state energy loss.

To understand the emission characteristics of solid-state **RBN-ICz**, a doped film with 5-(3-(4,6-diphenyl-1,3,5-triazin-2-yl)phenyl)-7,7-dimethyl-5,7-dihydroindeno[2,1-*b*]carbazole (DMIC-TRZ) as the host was prepared. The doped film exhibits red emission with a peak at 620 nm and a FWHM of 59 nm/0.19 eV (Fig. S23 and Table S2). Under a nitrogen atmosphere, the Φ_{PL} of the doped film reaches 96.3%. Compared with the spectrum in toluene solution, it appears a little red-shifted and broadened. This spectral change may be attributed to the strong host–guest interactions, especially the strong guest–guest interactions.[24] Transient PL measurement demonstrates that **RBN-ICz** exhibits a typical bi-exponential decay curve profile, in which the fast component and slow component correspond to prompt fluorescence and delayed fluorescence, respectively

Table 1 Summary of photophysical and electrochemical properties of *m*-Cz-BNCz and RBN-ICz

Compound	λ_{abs}^{a} [nm]	λ_{em}^{b} [nm]	FWHM^c [nm eV^{-1}]	E_{S1}^{d} [eV]	E_{T1}^{e} [eV]	ΔE_{ST}^{f} [eV]	E_g^{g} [eV]	HOMO^h [eV]	LUMO^h [eV]	Φ_{PL}^{i} [%]
***m*-Cz-BNCz**	484	519	38/0.18	2.50	2.42	0.08	2.42	−5.03	−2.63	97
RBN-ICz	582	615	44/0.15	2.13	1.96	0.16	2.00	−4.83^j	−2.83	90

[a] Peak wavelength of the lowest energy absorption band. [b] Peak wavelength of the PL spectrum in toluene (1×10^{-5} M, 298 K). [c] Full-width at half-maximum. [d] Singlet energy estimated from the onset of the fluorescence spectrum in toluene (1×10^{-5} M, 77 K). [e] Triplet energy estimated from the onset of the phosphorescence spectrum in the toluene matrix (1×10^{-5} M, 77 K). [f] $\Delta E_{ST} = E_{S1} - E_{T1}$. [g] Optical bandgap estimated from the absorption edge of the UV-vis spectrum. [h] Determined from cyclic voltammetry using the formula: $E_{LUMO} = -(E_{red} + 4.8)$ eV. [i] Absolute photoluminescence quantum yield measured with an integrating sphere system in N_2-bubbling toluene. [j] $E_{HOMO} = E_{LUMO} - E_g$.

Table 2 Summary of EL data of devices (host: DMIC-TRZ and sensitizer: PO-01) based on **RBN-ICz** with a 1 wt% doping concentration

Emitter	λ_{em}[a] [nm]	FWHM[b] [nm] [eV]$^{-1}$	CIE (x, y)[c]	V_{on}[d] [V]	L_{max}[e] [cd m^{-2}]	CE$_{max}$[f] [cd A^{-1}]	PE$_{max}$[g] [lm W^{-1}]	EQE[h] [%]
RBN-ICz	624	59/0.19	(0.67, 0.33)	2.8	54 810	32.3	39.5	34.1/20.5

[a] EL peak wavelength. [b] Full-width at half-maximum. [c] Commission Internationale de L'Eclairage coordinates (value taken at 100 cd m^{-2}). [d] Turn-on voltage at 1 cd m^{-2}. [e] Maximum luminance. [f] Maximum current efficiency. [g] Maximum power efficiency. [h] Maximum external quantum efficiency, and values at 1000 cd m^{-2}, respectively.

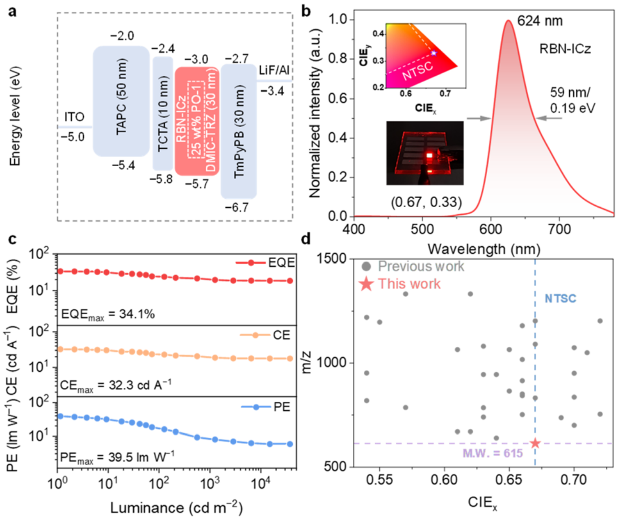

Fig. 5 EL characteristics of emitter **RBN-ICz**. (a) Molecular names and energy level diagram of materials used in the devices. (b) EL spectra. (c) EQE–*L*, CE–*L* and PE–*L* curves. (d) Summary of red OLED emitters: CIE$_x$ *vs.* molecular weight, comparing this work with previous reports.

(Fig. S24 and Table S3), with a prompt lifetime of 3.33 ns and a delayed lifetime of 209.9 μs, confirming its TADF characteristics. The TADF characteristics were further verified using the temperature-dependent transient PL decay spectra (Fig. S25). As the temperature increases from 100 K to 300 K, the proportion of the delayed fluorescence component gradually increases. Based on the Φ_{PL} value and the transient delayed lifetime data, the fluorescence radiative decay rate constant (k_r) and the RISC rate constant (k_{RISC}) were calculated (Table S3). Benefiting from the donor fused strategy of **RBN-ICz**, the molecular rigidity is significantly enhanced, which effectively improves the fluorescence radiative decay rate constant $k_r = 3 \times 10^8$ s^{-1}. This characteristic not only improves the radiative efficiency and suppresses non-radiative deactivation pathways, but also lays a solid foundation for achieving high-brightness and high-efficiency red emission.[25] These properties demonstrate that **RBN-ICz** has excellent TADF characteristics that can fully utilize excitons and suggest its potential for high optoelectronic performances in OLEDs.

Based on the excellent PL properties and high thermal stability of **RBN-ICz**, we systematically evaluated its EL performances by optimizing the OLED configuration through vacuum thermal evaporation: [ITO/(1,1-bis[(di-4-tolylamino)phenyl] cyclohexane] (TAPC) (50 nm)/tris(4-carbazolyl-9-ylphenyl)amine (TCTA) (5 nm)/DMIC-TRZ: *x* wt% **RBN-ICz** (30 nm)/3,3′-[5′-[3-(3-pyridinyl)phenyl]][1,1′:3′,1″-terphenyl]3,3″diyl]bispyridine (TmPyPB) (30 nm)/LiF/Al] ($x = 0.5, 1.0, 2.0$). Here, indium tin oxide (ITO) and Al are used as the anode and cathode, respectively. TAPC, TCTA, and TmPyPB serve as the hole transport layer (HTL), electron blocking layer (EBL) and electron transport layer (ETL), respectively, which effectively facilitate carrier injection and transport. DMIC-TRZ was selected as the host because it has been reported to exhibit bipolar transport with suitable energy levels, which can facilitate charge injection/transport (Fig. S26).[26] The corresponding EL performances including the current density (*J*), voltage (*V*), luminance (*L*), current efficiency (CE), power efficiency (PE), and compiled data are shown in Fig. S27 and Table S4 respectively.

All single-host devices exhibit similar low turn-on voltages of 2.6 V. Across all doping concentrations (0.5, 1.0 and 2.0 wt%), the devices emit red light with EL peaks ranging from 616 to 628 nm. The EL spectra are slightly red-shifted and broadened compared to the PL spectrum of **RBN-ICz** in dilute solution, which may be attributed to host–guest and guest–guest interactions induced by the rigid near-planar molecular geometry of **RBN-ICz.**[27] With the increasing doping concentration of **RBN-ICz**, the CIE coordinates shift from (0.66, 0.33) to (0.68, 0.32), which meets the red emission standard (0.67, 0.33) defined by the NTSC. At the optimal doping concentration of 1 wt%, the device demonstrates the best device performances with a maximum CE of 32.5 cd A^{-1}, a maximum PE of 39.2 lm W^{-1}, and a maximum EQE of 32.3%. Despite their high efficiency, single-host devices based on **RBN-ICz** suffer from drastic efficiency roll-off at high luminance levels. To address this issue, iridium(III) bis(4-phenylthieno-[3,2-*c*]pyridinato-N,C^2)acetylacetonate (PO-01) was introduced as an efficient phosphorescent sensitizer to activate red MR emitter **RBN-ICz**, which is expected to alleviate efficiency roll-off.[28] The decent spectral overlap between the emission of PO-01 and the absorption of **RBN-ICz** facilitates efficient energy transfer (Fig. S28), offering a promising route to mitigate efficiency roll-off.

The optimized 1 wt% doping concentration of **RBN-ICz** was selected as the terminal emitter, with 25 wt% of PO-01 incorporated as the sensitizer. The detailed device configuration and EL performance metrics are summarized in Table 2, Fig. 5, and S29. At a luminance of 100 cd m^{-2}, the EL spectrum exhibits a peak at 624 nm with a FWHM of 59 nm/0.19 eV and CIE coordinates of (0.67, 0.33), fully satisfying the NTSC red standard (Fig. 5b). These results demonstrate that in the red spectral region, the **RBN-ICz**-based OLED can achieve color purity comparable to that of micro-LED displays without the demand of optical filters or micro-cavity engineering (Fig. S30).[29] The sensitized device delivers a maximum EQE of 34.1%, a maximum CE of 32.3 cd A^{-1}, and a maximum PE of 39.5 lm

W^{-1}. Moreover, the EQE remains at 20.5% at a luminance of 1000 cd m^{-2}, indicating that the efficiency roll-off is effectively suppressed by the sensitization strategy (Fig. 5c). Notably, **RBN-ICz** represents the lowest molecular weight B,N-containing MR-TADF emitter reported so far in the red emission region (Fig. 5d and Table S5). These impressive EL properties highlight that the donor planarization strategy *via* intramolecular fusion is an effective route to efficient pure-red emission.

Conclusions

In conclusion, we construct **RBN-ICz** using a donor planarization strategy, achieved by intramolecular fusion of the donor into the BNCz core, enabling pure-red emission. Near-coplanarity (donor–core dihedral angle of 2.62°) extends π-conjugation and enhances LRCT properties, resulting in a 96 nm red shift (519 → 615 nm) and a narrowing of FWHM of 0.15 eV. The OLED based on **RBN-ICz** demonstrates pure-red emission (CIE: 0.67, 0.33) that complies with the NTSC standard red light, and the EQE reaches 34.1%. **RBN-ICz** represents the lowest molecular weight MR-TADF material reported so far in the red emission region. The planarized architecture retains low molecular weight and is compatible with vacuum thermal evaporation, overcoming the difficulty or instability of evaporation of red MR emitters due to their high molecular weight. These results establish donor planarization as a highly effective strategy for accessing a significant red shift while maintaining narrowband emission, thereby delivering structurally simple, highly efficient, pure-red MR-TADF emitters.

Author contributions

L. J. Li carried out most parts of the experiments and wrote the original manuscript. D. Y. Zhang analyzed the data and provided comments. Y. P. Qu was responsible for theoretical calculations. C. L. Li, Y. C. Xu and Y. Wang supervised the project, analyzed the data and revised the manuscript.

Conflicts of interest

There are no conflicts to declare.

Data availability

The data supporting this article are available in the supplementary information (SI).

Supplementary information: compound syntheses and characterization, other theoretical calculations, spectra and other device performance data. See DOI: https://doi.org/10.1039/d5sc09303a.

Acknowledgements

This work was supported by the National Natural Science Foundation of China (52173165 and 525B2044), the National Key R&D Program of China (2020YFA0714601), the Open Fund of the Key Lab of Organic Optoelectronics and Molecular Engineering of the Ministry of Education (53223000122), and the Fundamental Research Funds for the Central Universities. The authors also acknowledge the support of Laboratory of Flexible Electronics Technology, Tsinghua University.

References

1 (*a*) P. Pust, P. J. Schmidt and W. Schnick, *Nat. Mater.*, 2015, **14**, 454–458; (*b*) R. M. Soneira, *Inf. Disp.*, 2016, **32**, 26–31; (*c*) C. W. Tang and S. A. VanSlyke, *Appl. Phys. Lett.*, 1987, **51**, 913–915.

2 (*a*) R.-Z. An, F.-M. Zhao, C. Shang, M. Zhou and L.-S. Cui, *Angew. Chem., Int. Ed.*, 2025, **64**, e202420489; (*b*) C.-Z. Du, Y. Lv, H. Dai, X. Hong, J. Zhou, J.-K. Li, R.-R. Gao, D. Zhang, L. Duan and X.-Y. Wang, *J. Mater. Chem. C*, 2023, **11**, 2469–2474; (*c*) Y. Guo, W. Xie, Z. Ye, K. Xu, Z. Zhang, Z. Xiao, J. Miao, Y. Zou, C. Zhong, X. Yin, C. Yang and X. Cao, *Angew. Chem., Int. Ed.*, 2025, **64**, e202503320; (*d*) Y. Kondo, K. Yoshiura, S. Kitera, H. Nishi, S. Oda, H. Gotoh, Y. Sasada, M. Yanai and T. Hatakeyama, *Nat. Photonics*, 2019, **13**, 678–682; (*e*) B. Lei, Z. Huang, S. Li, J. Liu, Z. Bin and J. You, *Angew. Chem., Int. Ed.*, 2023, **62**, e202218405; (*f*) I. S. Park, H. Min and T. Yasuda, *Angew. Chem., Int. Ed.*, 2022, **61**, e202205684; (*g*) R. W. Weerasinghe, S. M. Suresh, D. Hall, T. Matulaitis, A. M. Z. Slawin, S. Warriner, Y.-T. Lee, C.-Y. Chan, Y. Tsuchiya, E. Zysman-Colman and C. Adachi, *Adv. Mater.*, 2024, **36**, 2402289; (*h*) Y. Yu, C. Wang, F.-F. Hung, C. Chen, D. Pan, C.-M. Che and J. Liu, *J. Am. Chem. Soc.*, 2024, **146**, 22600–22611; (*i*) J. Zhang, S. Zhang, C. Sun, R. Wang, Z. Guo, D. Cui, G. Tang, D. Li, J. Yuan, X. Lu, C. Zheng, W. Huang and R. Chen, *Adv. Mater.*, 2025, **37**, 2500953.

3 (*a*) Y.-C. Cheng, X. Tang, K. Wang, X. Xiong, X.-C. Fan, S. Luo, R. Walia, Y. Xie, T. Zhang, D. Zhang, J. Yu, X.-K. Chen, C. Adachi and X.-H. Zhang, *Nat. Commun.*, 2024, **15**, 731; (*b*) X.-C. Fan, K. Wang, Y.-Z. Shi, Y.-C. Cheng, Y.-T. Lee, J. Yu, X.-K. Chen, C. Adachi and X.-H. Zhang, *Nat. Photonics*, 2023, **17**, 280–285; (*c*) L. Hua, H. Wu, Z. Xia, M. Li, Y. Liu, S. Yan, W. Zhu, J. Y. Lee, Z. Ren and Y. Wang, *Adv. Mater.*, 2025, **37**, 2502180; (*d*) Y.-T. Lee, C.-Y. Chan, N. Matsuno, S. Uemura, S. Oda, M. Kondo, R. W. Weerasinghe, Y. Hu, G. N. I. Lestanto, Y. Tsuchiya, Y. Li, T. Hatakeyama and C. Adachi, *Nat. Commun.*, 2024, **15**, 3174; (*e*) J. Liu, Y. Zhu, T. Tsuboi, C. Deng, W. Lou, D. Wang, T. Liu and Q. Zhang, *Nat. Commun.*, 2022, **13**, 4876; (*f*) X.-F. Luo, S.-Q. Song, X. Wu, C.-F. Yip, S. Cai and Y.-X. Zheng, *Aggregate*, 2024, **5**, e445; (*g*) K.-K. Tan, W.-C. Guo, W.-L. Zhao, M. Li and C.-F. Chen, *Angew. Chem., Int. Ed.*, 2024, **63**, e202412283; (*h*) L. Wu, Z. Xin, D. Liu, D. Li, J. Zhang, Y. Zhou, S. Wu, T. Wang, S.-J. Su, W. Li and Z. Ge, *Adv. Mater.*, 2025, **37**, 2416224; (*i*) F. Zhang, V. Brancaccio, F. Saal, U. Deori, K. Radacki, H. Braunschweig, P. Rajamalli and P. Ravat, *J. Am. Chem. Soc.*, 2024, **146**, 29782–29791.

4 (*a*) L. Ge, W. Zhang, Y.-H. Hao, M. Li, Y. Liu, M. Zhou and L.-S. Cui, *J. Am. Chem. Soc.*, 2024, **146**, 32826–32836; (*b*) Y. Xu, Q. Wang, X. Cai, C. Li, S. Jiang and Y. Wang, *Angew.*

Chem., Int. Ed., 2023, **62**, e202312451; (*c*) W. Yang, J. Miao, F. Hu, Y. Zou, C. Zhong, S. Gong and C. Yang, *Adv. Funct. Mater.*, 2023, **33**, 2213056.

5 Y. Zhang, D. Zhang, T. Huang, A. J. Gillett, Y. Liu, D. Hu, L. Cui, Z. Bin, G. Li, J. Wei and L. Duan, *Angew. Chem., Int. Ed.*, 2021, **60**, 20498–20503.

6 (*a*) M. Hayakawa, X. Tang, Y. Ueda, H. Eguchi, M. Kondo, S. Oda, X.-C. Fan, G. N. I. Lestanto, C. Adachi and T. Hatakeyama, *J. Am. Chem. Soc.*, 2024, **146**, 18331–18340; (*b*) Q. Wang, T. Huang, Y. Qu, X. Song, Y. Xu and Y. Wang, *ACS Appl. Mater. Interfaces*, 2024, **16**, 4948–4957.

7 M. Yang, I. S. Park and T. Yasuda, *J. Am. Chem. Soc.*, 2020, **142**, 19468–19472.

8 Y. Zou, M. Yu, Y. Xu, Z. Xiao, X. Song, Y. Hu, Z. Xu, C. Zhong, J. He, X. Cao, K. Li, J. Miao and C. Yang, *Chem*, 2024, **10**, 1485–1501.

9 (*a*) K. R. Naveen, J. H. Oh, H. S. Lee and J. H. Kwon, *Angew. Chem., Int. Ed.*, 2023, **62**, e202306768; (*b*) X. Wu, C.-H. Wang, S. Ni, C.-C. Wu, Y.-D. Lin, H.-T. Qu, Z.-H. Wu, D. Liu, M.-Z. Yang, S.-J. Su, W. Zhu, K. Chen, Z.-C. Jiang, S.-D. Yang, W.-Y. Hung and P.-T. Chou, *J. Am. Chem. Soc.*, 2024, **146**, 24526–24536; (*c*) H.-X. Ni, X.-F. Luo, L. Yuan, J.-J. Hu, W.-W. Zhang and Y.-X. Zheng, *J. Mater. Chem. C*, 2024, **12**, 2578–2584.

10 (*a*) T. Hua, X. Cao, J. Miao, X. Yin, Z. Chen, Z. Huang and C. Yang, *Nat. Photonics*, 2024, **18**, 1161–1169; (*b*) Z. Liu, L. Meng, Y. Jiang, C. Li, H. Gu, K. Zhao, J. Zhang, H. Meng and Y. Ren, *J. Am. Chem. Soc.*, 2025, **147**, 3650–3661.

11 Y. Wu, J. Liu, G. Yang, Z. Bin and J. You, *J. Am. Chem. Soc.*, 2025, **147**, 19305–19314.

12 Z. Yang, D. Liu, X. Cheng, T. Wang, Z. Li, G.-X. Yang, Z. Chen, J. Hu, Y. Fu, X. Nie, Y. Ren, Y. Zeng, Y. Chen, K. Liu, M. Li and S.-J. Su, *Angew. Chem., Int. Ed.*, 2025, **64**, e202423602.

13 (*a*) C. Cheng, S. Zhu, H. Zhang, T. Huang, C. Li, Z. Chen, P. Xu, R. Liu, X. Cao, L. Wang, D. Zhang and L. Duan, *Angew. Chem., Int. Ed.*, 2025, **64**, e202504628; (*b*) T. Hatakeyama, K. Shiren, K. Nakajima, S. Nomura, S. Nakatsuka, K. Kinoshita, J. Ni, Y. Ono and T. Ikuta, *Adv. Mater.*, 2016, **28**, 2777–2781; (*c*) X. Song, G. Lu, Y. Man, J. Zhang, S. Chen, C. Han and H. Xu, *Angew. Chem., Int. Ed.*, 2023, **62**, e202300980.

14 Z. Pei, Q. Ou, Y. Mao, J. Yang, A. de la Lande, F. Plasser, W. Liang, Z. Shuai and Y. Shao, *J. Phys. Chem. Lett.*, 2021, **12**, 2712–2720.

15 (*a*) Y. Sano, T. Shintani, M. Hayakawa, S. Oda, M. Kondo, T. Matsushita and T. Hatakeyama, *J. Am. Chem. Soc.*, 2023, **145**, 11504–11511; (*b*) W. Yuan, Q. Jin, M. Du, L. Duan and Y. Zhang, *Adv. Mater.*, 2024, **36**, 2410096.

16 J. Kang, D. J. Shin and J. Y. Lee, *Adv. Opt. Mater.*, 2025, **13**, 2402653.

17 M. Xiao and T. Lu, *J. Adv. Phys. Chem.*, 2015, **4**, 111–124.

18 S. Wu, W. Li, K. Yoshida, D. Hall, S. Madayanad Suresh, T. Sayner, J. Gong, D. Beljonne, Y. Olivier, I. D. W. Samuel and E. Zysman-Colman, *ACS Appl. Mater. Interfaces*, 2022, **14**, 22341–22352.

19 T. Lu, *J. Mol. Model.*, 2021, **27**, 263.

20 J. Zhang and T. Lu, *Phys. Chem. Chem. Phys.*, 2021, **23**, 20323.

21 T. Lu and Q. Chen, *Theor. Chem. Acc.*, 2020, **139**, 25.

22 L. Li, T. Huang, Y. Xu, Y. Qu, W. Cui, L. Xu, C. Li and Y. Wang, *Angew. Chem., Int. Ed.*, 2025, **64**, e202504002.

23 X.-C. Fan, F. Huang, H. Wu, H. Wang, Y.-C. Cheng, J. Yu, K. Wang and X.-H. Zhang, *Angew. Chem., Int. Ed.*, 2023, **62**, e202305580.

24 J.-J. Hu, X. Liang, Z.-P. Yan, J.-Q. Liang, H.-X. Ni, L. Yuan, J.-L. Zuo and Y.-X. Zheng, *Angew. Chem., Int. Ed.*, 2025, **64**, e202421102.

25 (*a*) K. Jiang, X. Chang, J. Zhu, T. Zhu, J. Yu, Y. Wang, Y. Zhang, D. Ma and W. Zhu, *Angew. Chem., Int. Ed.*, 2025, **64**, e202421520; (*b*) L. Xing, J. Wang, W.-C. Chen, B. Liu, G. Chen, X. Wang, J.-H. Tan, S. S. Chen, J.-X. Chen, S. Ji, Z. Zhao, M.-C. Tang and Y. Huo, *Nat. Commun.*, 2024, **15**, 6175.

26 D. Zhang, C. Zhao, Y. Zhang, X. Song, P. Wei, M. Cai and L. Duan, *ACS Appl. Mater. Interfaces*, 2017, **9**, 4769–4777.

27 (*a*) H. Chen, M. Du, C. Qu, Q. Jin, Z. Tao, R. Ji, G. Zhao, T. Zhou, Y. Lou, Y. Sun, W. Jiang, L. Duan and Y. Zhang, *Angew. Chem., Int. Ed.*, 2024, **64**, e202415400; (*b*) C. Murawski, K. Leo and M. C. Gather, *Adv. Mater.*, 2013, **25**, 6801–6827.

28 W. C. Guo, W. L. Zhao, K. K. Tan, M. Li and C. F. Chen, *Angew. Chem., Int. Ed.*, 2024, **63**, e202401835.

29 E.-L. Hsiang, Z. Yang, Q. Yang, Y.-F. Lan and S.-T. Wu, *J. Soc. Inf. Disp.*, 2021, **29**, 446–465.